Ultrafast Orbital Depolarization and Defect-Localized Phonon Dynamics Induced by Quantum Resonance between Multi-Nitrogen Vacancy Defects

I-Ya Chang and Kim Hyeon-Deuk*

Department of Chemistry, Kyoto University, Kyoto, 606-8502, Japan

E-mail: kim@kuchem.kyoto-u.ac.jp

*To whom correspondence should be addressed

Abstract

Proximate nitrogen-vacancy (NV) defects with inter-defect interaction may establish a new kind of quantum qubit network to explore controlled multi-body quantum dynamics. Especially, by introducing the critical distance and favorable orientation between a pair of NV defects, the quantum resonance (QR) can be induced. Here, we present the first real-time depolarization and phonon dynamics on the excited state at ambient temperature which are intrinsic to the proximate multi-NV defects. We computationally demonstrated that the QR can effectively change the major properties of the multi-NV defects such as orbital degeneracy, orbital delocalization, local phonon modes, electron-phonon coupling, and orbital depolarization dynamics, elucidating the physical mechanisms and finding the key factors to control them. The physical insights provide a starting point for the positioning accuracy of NV defects and creation protocols with broad implications for magnetometry, quantum information, nanophotonics, sensing and spectroscopy, letting the QR be a new kind of physical manipulation.

TOC Graphic.

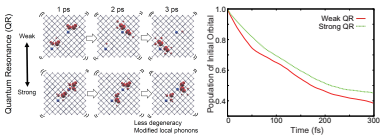

Diamond can stably accommodate a point defect called the nitrogen-vacancy (NV) defect composed of a nitrogen substitution with a nearest-neighbor vacancy.[1–10] The NV defect is a leading candidate of building blocks for future quantum computers[11–14] and nanoscale sensor devices[15–19] because of the promising spin and optical properties, *e.g.* spin coherences of one second at room temperature and their precise quantum control for individual NV defect. Proximate NV defects with inter-defect interaction may further establish a new kind of quantum qubit network in solids and can be a fruitful test to explore controlled multi-body quantum dynamics.[4,20–26] Recent advances in the ion implantation method,[19,22,27–30] which is a widely employed strategy to create an NV defect at a precisely controlled location, have made it possible to create more proximate NV defects in a diamond crystal that may interact with each other. Elucidating how proximate NV defects interact and change intrinsic properties of each NV defect is actually becoming a key challenge. Concentration of NV defects drastically changes spin depolarization dynamics,[4,31] NV ionization rates,[21] carrier dynamics under photoexcitation,[32,33] and spectroscopy like fluorescence.[21,34–36] Even applications to heralded two-NV-defect quantum gates[24] as well as the magnon condensation due to dense ensemble of NV defects[4] were recently proposed. However, despite its paramount importance in utilizing this new kind of properties in interacting NV defects, the possibilities and roles are not fully understood yet. There is further possibility of the multi-NV defects: By introducing the critical nanoscale distance and favorable orientation between a pair of NV defects, the quantum resonance (QR) can be induced owing to the short-range strong interaction between two NV defects which is physically different from the longer-range dipole-dipole interaction.[37] The QR should more effectively change the major properties of NV defects such as orbital degeneracy, local phonon modes, electron-phonon couplings, and spin and orbital depolarization dynamics due to the stronger inter-defect interaction.

The NV defect is just like a soft molecule embedded in a diamond crystal, and thus undergoes a significant structural change and phonon modification by photoexcitation at ambient temperature *e.g.* the zero-phonon line became lowered compared to the lowest vertical ab-

sorption energy through nuclear relaxation on the ES while the phonon spectrum and the ES orbital dynamics depend on the temperature.[1,10,38–47] In order to fully elucidate ultrafast picosecond and femtosecond non-radiative dynamics appearing in the NV defect,[42,44,48] the effects of temperature to cause thermal fluctuations,[49,50] vibrational phonon modes localized around the NV defect,[43,45,48,51–53] and electron-phonon couplings influencing non-adiabatic (NA) transition dynamics[42,45,48,54–57] as well as the Jahn-Teller (JT) distortion[50,57] are all important. We recently developed a new computational method to simulate real-time NA photoexcited dynamics of electron occurring in the single NV defect embedded in a diamond crystal at ambient temperature based on an ab initio molecular dynamics (AIMD) simulation.[42] The simulations successfully reproduced the experimentally observed ultrafast component of the orbital depolarization decay of 100 fs as well as the slower component of 10 ps including the temperature dependence. The orbital depolarization dynamics dominates ultrafast electron dynamics occurring in the NV defect on the excited state (ES) after photoexcitation,[42,48] and will be referred simply as the depolarization below.

In this letter, we present the first real-time depolarization and phonon dynamics on the ES at ambient temperature which are intrinsic to the proximate multi-NV defects exhibiting the short-range QR. We extended our previous computational method mentioned above to specifically extract and calculate time-dependent orbital energies and electron-phonon couplings of relevant electron spin only. In particular, we characterized the ultrafast depolarization and local phonon modes varying inter-defect distance and orientations, which allows us to elucidate the physical mechanisms and to find the important key factors such as critical nanoscale distance and favorable orientation to control its properties.

In order to discuss effects of the QR between the multi-NV defects, we introduce two NV defects which are placed with the different inter-defect distances and orientations. The total charge of the NV diamond cell was set to be -2. Figure 1 shows the stable structures of the multi-NV defects in the diamond crystal, L_3, L_1 and L'_1, optimized on the ES. Note that the two NV defects are not on the diagonal axis of the diamond cell. Our guiding principle to

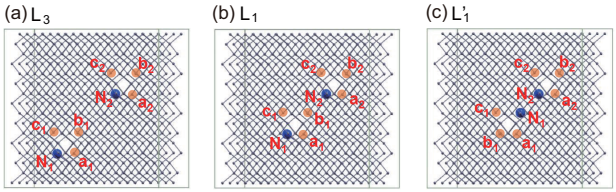

Figure 1: Optimized geometries of (a) L_3, (b) L_1 and (c) L'_1 on the ES. The periodic supercell contains two N atoms and 508 C atoms. Each NV defect is composed of one vacancy site and four closest atoms, one N atom (blue) and three C atoms (orange), which are labeled as N_1, a_1, b_1 and c_1 for the first NV defect and N_2, a_2, b_2 and c_2 for the second NV defect, respectively.

design the multi-NV diamond is placing the two pairs of the NV defects as close as possible to the center of the diamond cell with the same N-V bond direction. (See Computational Method in Supporting Information) We hereafter focus on the defect orbitals which have a down-spin electron because the defect orbitals which have an up-spin electron as well as the valence band (VB) are fully occupied and quiet here while the ES NA transition dynamics related to depolarization happens only among the electron down-spin defect orbitals involving their occupied and unoccupied orbitals. The six electron down-spin defect orbitals are numbered from 1019 to 1024 in the order of the lower orbital energy. All the orbitals discussed below refer only to electron down-spin orbitals and will be simply expressed as orbitals unless otherwise stated. The ES was made by exciting a down-spin electron from the highest-energy occupied orbital, the orbital 1020, up to the first unoccupied orbital, the orbital 1021. L_3 has the longer inter-defect distance and should exhibit the weaker QR between the two NV defects while L_1 has the shorter inter-defect distance and should exhibit the stronger QR compared to L_3. L'_1 has the same inter-defect distance as L'_1s while the two NV defects are oppositely orientated so that the two N atoms are aligned between the two vacancies blocking the QR, which reduces the extent of the QR. We emphasize that total density of NV defects in a diamond crystal does not need to be extremely high here because only a single pair of two NV defects is necessary to achieve the present QR.

We performed the real-time AIMD simulations of L_3, L_1 and L'_1 on the ES at 300 K.(See

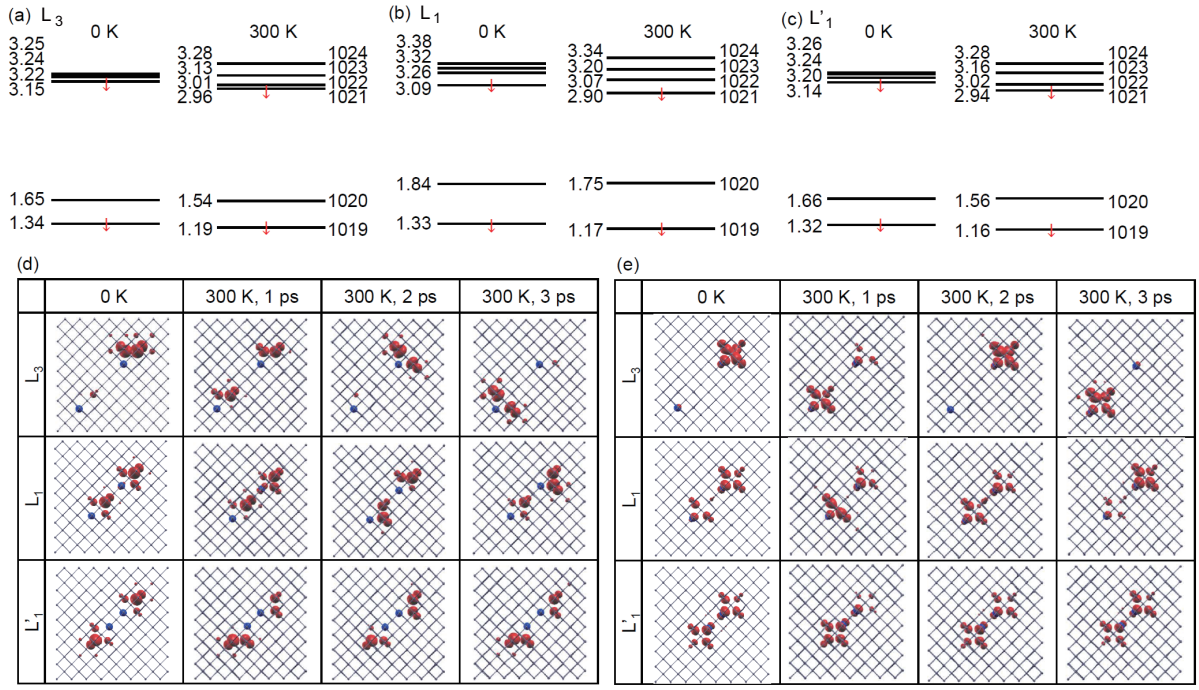

Figure 2: Defect orbital energies relative to the highest energy of the VB orbitals of (a) L_3, (b) L_1 and (c) L'_1 optimized on the ES at 0 K and the averages of the real-time orbital energies fluctuating at 300 K. The unit is eV. Defect orbitals (d) 1021 and (e) 1020 optimized on the ES at 0 K and the corresponding time-dependent defect orbitals at 1 ps, 2 ps and 3 ps during the ES AIMD simulations at 300 K. The defect orbitals were visualized by XCrySDen2 with the isovalue of 0.025.

Computational Method in Supporting Information) Our computational method takes into account the JT distortion and phonon dynamics modified on the ES, and also the time- and orbital-dependent electron-phonon coupling and their thermal modulations at the ambient temperature. The time- and orbital-dependent electron-phonon coupling, which would never appear under the Born-Oppenheimer approximation with stationary atoms, plays a critical role in determining the ES NA transition dynamics among the defect orbitals which are the main focus of the current study. The phonon modes and electron-phonon couplings related to the multi-NV defects on the ES and on the ground state (GS) should be different especially at the ambient temperature, requiring the current real-time MD simulations on the ES at 300 K.[48,54]

We obtained the stable temperature fluctuations around 300 K in the ES AIMD simulations of L_3, L_1 and L'_1.(Fig. S1) The stable temperature fluctuations support that the L_3, L_1 and L'_1 systems can stably exist and modulate even on the ES at the ambient temperature; the current stable temperature fluctuations would not be realized if the structures were unstable or fragile. Actually, the thermal structural disorder at 300 K is quite small in any of the L_3, L_1 and L'_1 cases, indicating the stable structural modulations around the ES structure at 0 K. (Table S1) Such structural modulations directly lead to the stable fluctuations of the orbital energies of L_3, L_1 and L'_1 on the ES at 300 K. (Fig. S2) The significantly fluctuating energies of each NV defect orbital at the ambient temperature affect the ES NA transition dynamics among the defect orbitals, which will be discussed in Fig.5.

Figs.2(a)-2(c) show the ES orbital energies of L_3, L_1 and L'_1 optimized at 0 K and the averages of the real-time orbital energies fluctuating at 300 K shown in Fig. S2. The energies of the orbitals 1022-1024 become less degenerate in L_1 than in L_3 and L'_1 at 0 K. The stronger QR induced between the two proximate NV defects in L_1 causes a stronger coupling among the defect orbitals, leading to the more split and less degenerate higher-energy orbitals in L_1. However, even the more degenerate higher-energy orbitals 1022-1024 in L_3 and L'_1 at 0 K become less degenerate at 300 K due to the thermal modulation of the orbital energies

at the ambient temperature. In addition, the patterns of the GS orbital energies at 0 K are more similar to the patterns of the ES orbital energies at 0 K rather than to the patterns of the ES orbital energies averaged at 300 K; the higher-energy orbitals, 1021-1024, are more degenerate at 0 K both on the GS and ES compared to the ES orbital energies averaged at 300 K although the degeneracy is slightly more apparent on the GS than on the ES. (Fig. S3) The degeneracy of the higher-energy orbitals, which is important for the ultrafast depolarization through the NA transition dynamics among them, is influenced not only by the QR but also by the ambient temperature.

The optimized defect orbitals of L_3, L_1 and L'_1 on the GS and ES at 0 K and the time-dependent defect orbitals of their instantaneous structures at 1 ps, 2 ps and 3 ps along the ES AIMD simulations at 300 K are shown in Figs. S4-S6. (See also Table S2 and Fig. S3) The orbitals 1021 and 1020 on the ES are especially extracted and shown in Figs.2(d) and 2(e), respectively. In L_3 which has the weaker QR because of the longer inter-defect distance, the defect orbitals are relatively more localized at one of the two NV defects. (Fig. S4) It is remarkable that the localized orbitals actively change positions and/or shapes of the lobes and alter from one to another NV defect with time due to the thermal modulations of the flexible inter-defect structure in L_3. The active altering of the electron-excited orbital 1021 can be the main origin of the ultrafast depolarization in L_3. In addition to the higher-energy orbitals 1021-1024, the lower-energy orbitals 1019 and 1020 also exhibit the active orbital altering in L_3, which is qualitatively different from the L_1 and L'_1 cases as will be explained below. The orbital altering is most active in L_3 because more C atoms aligned between the two NV defects give the more flexibility to the inter-defect structure. In fact, the average structural disorder between the GS and the ES at 0 K corresponding to the JT distortion is larger in L_3 than in L_1 and L'_1.(Table S1) In spite of the active changes of the orbitals, the lower-energy orbitals 1019 and 1020 always form a complementary pair to symmetrically balance each other while the higher-energy orbitals 1021-1024 form another group to make their orbitals symmetric in total. Since L_1 possesses the stronger QR induced by the shorter

inter-defect distance, its orbitals tend to be more delocalized over the two NV defects even on the ES. (Fig. S5) Such delocalized orbitals of L_1 are more stable than the localized orbitals in L_3 especially in the cases of the lower-energy orbitals 1019 and 1020; the delocalized orbitals of L_1 do not significantly change their lobe shapes even at 300 K as often as the localized orbitals of L_3 in spite of the larger energy fluctuations of the lower-energy orbitals. (Fig. S2) It is important that the orbital 1021 can keep its original lobe shape better in L_1, suppressing the depolarization caused by the orbital altering. The better-kept orbitals stemmed from the fewer C atoms between the two NV defects and the resulted fewer structural variations in L_1. (Table S1) In contrast, the higher-energy orbitals 1022-1024 change their lobe shapes and locations with time even in L_1, which could contribute to the depolarization. In L'_1 which has the shorter inter-defect distance but the vacancy defects pointing away from each other, the higher-energy defect orbitals 1021-1024 simultaneously exist at both of the two vacancies but they are separated away from each other due to blocking by the two N atoms.(Fig. S6) The orbital 1021 of L'_1 does not largely change its lobe shape while the higher-energy orbitals 1022-1024 appearing around the vacancies change their shapes and locations of the lobes with time like the L_1 case. Those changes can also cause the depolarization through the effective NA transitions among the orbitals starting from the orbital 1021. The significant altering in the defect orbitals on the ES at 300 K is not caused by the JT distortion which can happen even at 0 K but by the thermal fluctuations of the flexible NV defect structures at the ambient temperature. The defect orbitals are just like molecular orbitals formed by two soft molecules embedded in the solid diamond crystal, and the atomic motions around the flexible NV defects can affect the time-dependent defect orbitals, which contributes to the ultrafast depolarization dynamics.

We Fourier-transformed the real-time fluctuations of the defect orbital energies of L_3, L_1 and L'_1 on the ES at 300 K shown in Fig. S2. The obtained power spectra in Fig.3 thus show the typical phonon modes involved in the flexible multi-NV defect structures and directly related to the energy fluctuations of the defect orbitals. The power spectra of the

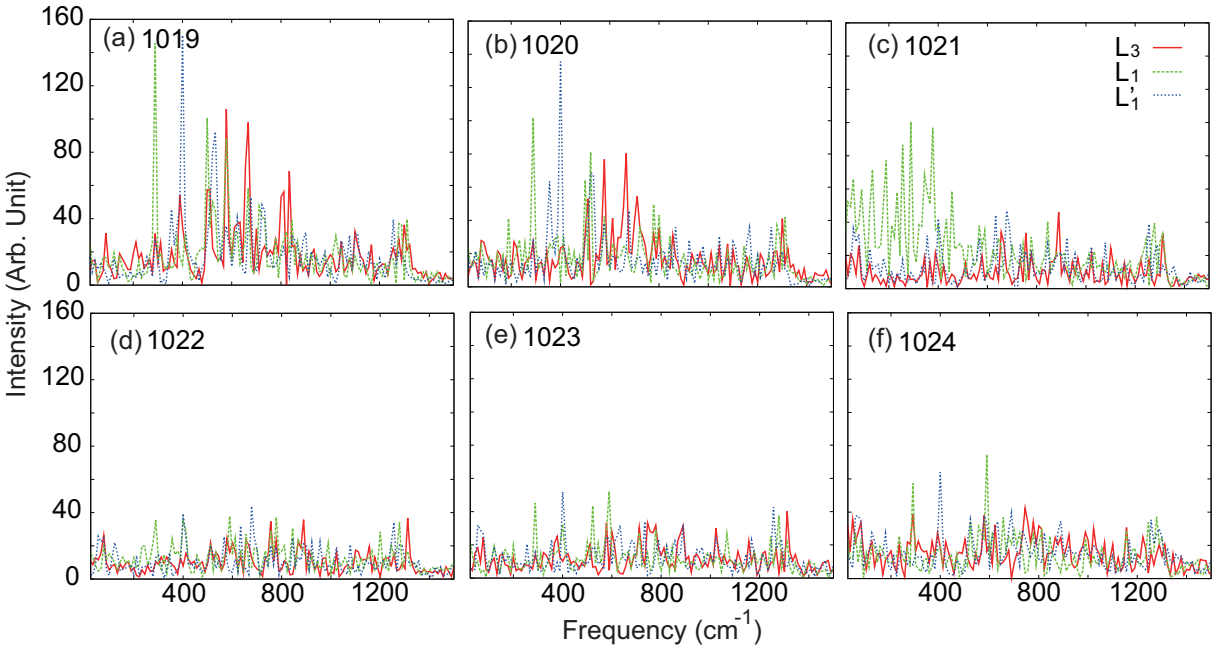

Figure 3: Power spectra of the real-time defect orbital energies on the ES at 300 K.

orbitals 1019 and 1020 have the strongest intensity among the six defect orbitals reflecting their strongest energy fluctuations in Fig. S2; the orbitals 1019 and 1020 which embrace all the defect core atoms are most influenced by the real-time atomic motions of the whole flexible NV defects. It should be noted that the power spectra exhibit peaks around 1300 cm^{-1} which is close to the experimentally observed Raman peak frequency of a diamond crystal, 1330 cm^{-1}.[1,8] The current simple power spectra of the defect orbital energies still can reproduce such representative Raman mode.

In addition to the high-frequency Raman peak, there are three significant low-frequency peaks appearing in the power spectra of the defect orbital energies: the sharp peak around 260-290 cm^{-1}, the sharp peak around 350-400 cm^{-1}, and the broad peak around 500-590 cm^{-1}. These frequency ranges are in harmony with the experimentally observed frequency components like 259 cm-1,[48] 355 cm-1,[51] 558 cm-1,[48] and 560 cm-1.[58] The power spectra directly obtained by Fourier-transforming the real-time vibrational dynamics of N-V and C-V on the ES at 300 K demonstrate such local phonon modes formed around the NV

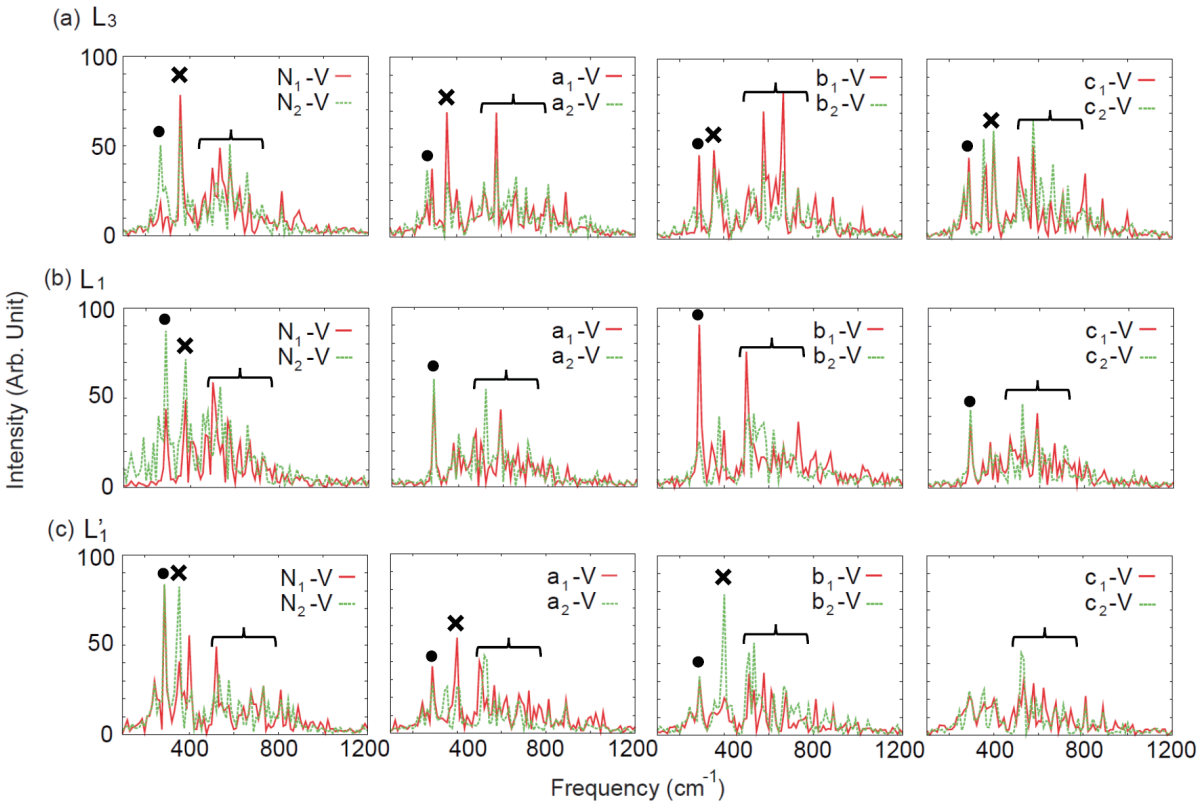

Figure 4: Power spectra of the real-time vibrational dynamics involved in the flexible NV defects of (a) L_3, (b) L_1 and (c) L'_1 on the ES at 300 K. The typical vibrations included in the two NV defects, two N-V vibrations and six C-V vibrations, were Fourier-transformed. The atomic names in each panel correspond to the labeling in Fig.1. We marked the sharp peaks around 260-290 cm^{-1} with a black dot ($\cdot$), the sharp peaks around 350-400 cm^{-1} with a black cross ($\times$), and the broad peaks around 500-590 cm^{-1} with a curly ket } only when they are significant.

defects, which is consistent with the previous reports that phononic vibrational modes are quasi-localized in the vicinity of the NV defect.[42,45,48,54] (Fig.4) As shown in Fig.4(a), all the power spectra of the local vibrations around the NV defects of L_3 actually exhibit the three typical peaks corresponding to the three low-frequency peaks appearing in the power spectra of the defect orbital energies in Figs.3(a) and 3(b). The broad peaks around 500-590 cm^{-1} have the larger intensity and appear almost equally in L_3 where the two NV defects are more independent, indicating that this broad peak stems from a collective local phonon mode of each single NV defect equally involving all the N and C atoms like a shrinking mode of the whole NV defect. The phonon intensity becomes weaker in L_1 and L'_1 because the collective local phonon mode of each NV defect is slightly collapsed due to the stronger QR. The sharp 260-290 cm^{-1} peaks exhibit the larger intensity in L_1. Because L_1 has the shortest distance between the C atom of the first NV defect, b_1, and the N atom of the second NV defect, N_2, electron around b_1 can be attracted more to N_2. (Fig.1(b)) The peaks of 260-290 cm^{-1} then should be assigned as a phonon mode involving such electron-poor C atom. In fact, the vibrations involving the two atoms, N_2-V and b_1-V, exhibit the largest intensity among the 260-290 cm^{-1} peaks as seen in Fig.4(b). Note that an electron-poor C atom originally exists even in a single NV defect because of the proximity of the N and C atoms like N_1 and a_1, as evidenced by the 260-290 cm^{-1} peaks appearing in Figs.4(a) and 4(c) for L_3 and L'_1, respectively. The stronger QR induced in L_1 just enhanced the 260-290 cm^{-1} phonon mode by generating the additional electron-poorer C atom. In contrast, the sharp 350-400 cm^{-1} peaks become weaker in L_1 while they are apparent in L_3 and L'_1. Based on these facts, the local defect mode of 350-400 cm^{-1} should involve a C atom which is less influenced by an N atom and can keep electron better. In spite of the shorter inter-defect distance, L'_1 can have such less influenced C atoms, *e.g.* b_1 and b_2, as well as L_3 due to the opposite orientation of N-b_1 and N-b_2. (Fig.1(c)) The blue-shifted 350-400 cm^{-1} peaks compared to the 260-290 cm^{-1} peaks also support the current picture; electron of the C atom, b_1, should be richer in the 350-400 cm^{-1} vibration than in the 260-290 cm^{-1} vibration. The reason why

the representative local phonon modes appear only in the power spectra of the orbitals 1019 and 1020 can be explained by the fact that the orbitals 1019 and 1020 embrace all the defect core atoms and their orbitals are most influenced by the real-time vibrational dynamics of the whole flexible NV defects. The different geometries of the multi-NV defects, L_3, L_1 and L'_1, can enhance or suppress the local phonon modes of different frequencies depending on the QR, which proposes that the extent of the QR between the multi-NV defects can be detected through the intensity of the local phonon modes.

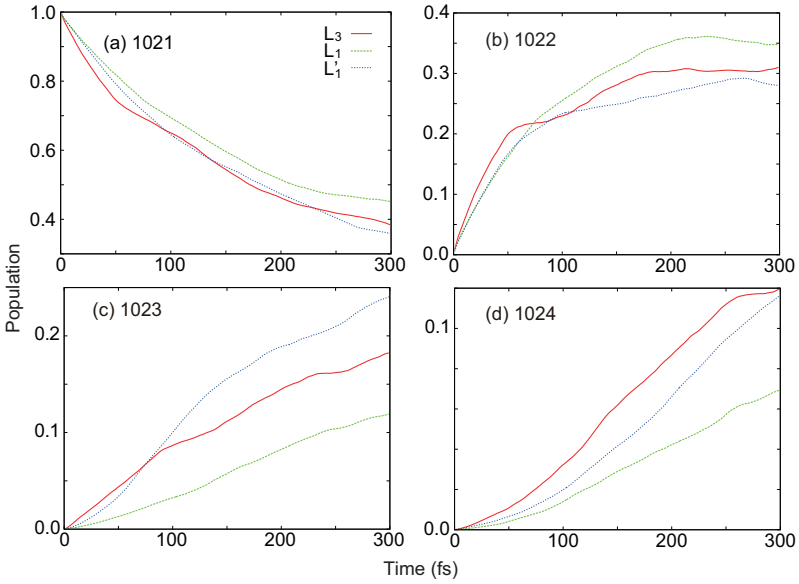

Figure 5: Real-time population dynamics of the defect orbitals (a)1021, (b)1022, (c)1023 and (d)1024 caused by the NA transitions occurring in L_3, L_1 and L'_1. The orbital 1021 was initially populated by exciting an electron from the orbital 1020, which is the possible lowest-energy excitation. The deexcited population down to the orbital 1020 is negligible while the orbital 1019 is already occupied.

The NA dynamics simulations among the defect orbitals were performed with the time-dependent electron-phonon couplings and defect orbital energies.[59–65] (See Computational Method in Supporting Information) The current NA transition dynamics is spin-dependent and takes place only among the defect orbitals which have down-spin electrons. Figure 5 shows the time-dependent population of the ES defect orbitals 1021-1024 in L_3, L_1 and L'_1. The population dynamics starts from the initially excited orbital 1021. We obtained the

almost converged population dynamics in the shown time region by averaging over 2700 different initial conditions. Each population dynamics, which started from a different initial time, differs from each other depending on the instantaneous initial condition caused by the thermal modulations of the orbital energies and electron-phonon couplings at 300 K. If the effects of the thermal modulations were small enough and each population dynamics was similar to each other regardless of the initial conditions, we could get the converged population dynamics with much fewer initial samples. The fact that a few thousands of initial samples are required to get the converged results means that the thermal modulations depending on each moment essentially influence each NA transition dynamics, making the initial-time averages hard to converge.

As Fig.5(a) shows, the population of the initially excited orbital 1021 decays more slowly in L_1 than in L_3 and L'_1. Reminding that the lobe shape of the orbital 1021 does not significantly change in L_1 as shown in Fig.2(d), the polarization initially created in L_1 should last longer. In L_3, the lobes of the orbital 1021 actively alters with time as shown in Fig.2(d) and, moreover, its population decays faster than L_1, leading to its faster depolarization. Although the orbital 1021 of L'_1 also keeps its lobe shape well as shown in Fig.2(d), L'_1 exhibits the faster population decay of the initially excited orbital 1021 than L_1, which results in the faster depolarization compared to the L_1 case. Summarizing the above results, the stronger the QR is, the slower the initial polarization decay is. We therefore conclude that the strong QR can suppresses the depolarization dynamics and keeps the initial polarization well. As shown in Fig.5(a), there is little difference between L_3 and L'_1 in the main NA transition dynamics, indicating that controlling both of the distance and orientation between the multi-NV defects is crucial to induce the new functionality owing to the QR. Fig.5(b) shows that the NA transition to the nearest orbital 1022 is more effective in L_1 than in L_3 and L'_1. Instead, L_3 and L'_1 exhibit the more population flows to the higher-energy orbital 1023 and 1024 compared to L_1 as Figs.5(c) and 5(d) show. These nontrivial population dynamics depending on L_3, L'_1 and L_1 can be explained by a combination of the non-degeneracy of the

orbitals caused by the QR and the electron-phonon couplings between the defect orbitals. In fact, it has been reported that not only defect orbital energies but also electron-phonon couplings essentially influence ES dynamics among defect orbitals and their optical response including a lineshape.[42,48,54]

Table 1: Electron-phonon couplings in the unit of meV between the initially excited orbital 1021 and the energetically close three defect orbitals.

orbital number	L_3	L_1	L'_1
1022	67.6	61.7	51.4
1023	15.4	7.31	9.39
1024	6.46	4.51	6.73

Table 1 lists the time-averaged electron-phonon couplings between the initially excited orbital 1021 and the defect orbitals 1022-1024 which are energetically close to the orbital 1021. The values are root mean squares of time-dependent electron-phonon couplings during the 3 ps ES AIMD simulations at 300 K. L_3 has the higher degeneracy in the defect orbitals due to the weaker QR, and also has the relatively large electron-phonon coupling to all the orbitals. Thus, the population decay of the initially excited orbital 1021 is faster and the population increases of not only the nearest orbital 1022 but also the higher-energy orbitals 1023 and 1024 are totally large. The lower degeneracy of the defect orbitals in L_1 due to the stronger QR rationalizes its slower population decay of the initially excited orbital 1021. However, as Table 1 shows, the electron-phonon coupling to the nearest orbital 1022 is much larger than the electron-phonon couplings to the higher-energy orbitals 1023 and 1024 in L_1, making most of the initial population flow into the nearest orbital 1022 in L_1. L'_1 has the higher degeneracy in the defect orbitals than L_1, and has the larger electron-phonon couplings to the higher-energy orbitals 1023 and 1024 than L_1, leading to the more population flow to the higher-energy orbitals in L'_1 than in L_1. In any case, the population hardly flows into the originally electron-occupied orbital 1020 because of the largest energy gap between the initially excited orbital 1021 and the orbital 1020. The root mean squares of the time-dependent electron-phonon couplings among all the defect orbitals are calculated

as 24.1 meV in L_3, 26.9 meV in L_1, and 25.7 meV in L'_1. The difference is small and L_1 has the even slightly larger electron-phonon coupling than L_3 and L'_1, which itself can not rationalize the suppressed depolarization dynamics in L_1, suggesting that not the simply averaged but the time- and orbital-dependent electron-phonon couplings are indispensable to explain the present NA transition dynamics among the defect orbitals. We also note that not only a transition from the initially excited orbital 1021 but also transitions among all the ES defect orbitals are involved in the current NA dynamics simulations. Therefore, the actual NA transition dynamics could be more complicated than the above scenario.

In summary, we computationally demonstrated that the strong QR induced by the short-range defect interaction can effectively change the major properties of the multi-NV defects such as orbital degeneracy and delocalization, phonon modes localized around the multi-NV defects, and orbital-dependent electron-phonon couplings to cause the NA transition dynamics among the defect orbitals. Especially, by identifying the critical nanoscale distance and favorable orientation between a pair of the NV defects, we concluded that the ultrafast orbital depolarization is suppressed and the initial polarization information is better-kept by the stronger QR. The higher polarization fidelity facilitates coupling of NV photon sources to plasmonic waveguides and increases the interference visibility of single photons emitted by the multi-NV defects, leading to the use of the polarization state as an additional variable in quantum information processing. The short-range QR is physically different from the longer-range dipole-dipole interaction, and will not suffer from the long-range rapid charge fluctuation and additional dipole-dipole interactions which can be a source of the decoherence of each NV spin state. The QR can be a new kind of physical manipulation to the NV defect in addition to the previous means like magnetic and electric fields, strain, temperature and pressure. The physical insights obtained in this study indicate that precisely controlling both of the nanoscale distance and orientation between the multi-NV defects is crucial to induce the new functionality owing to the QR. The above conclusions are broadly applicable to many other solid-state defects of potential technological importance such as silicon-vacancy

in diamond and divacancy in silicon carbide, providing a starting point for the positioning accuracy of defects and creation protocols with broad implications for magnetometry, quantum information, nanophotonics, sensing and ultrafast spectroscopy.

Acknowledgments

K.H.-D. acknowledges the financial supports from JST (PRESTO), Toyota Mobility Foundation, and Grant-in-Aid for Scientific Research on Innovative Areas, Grant No.18H05407.

Supporting Information. Detailed data on temperatures, orbitals, energies, lattice parameters, structures and the computational methods.

References

(1) Czelej, K.; Ćwieka, K.; Śpiewak, P.; Kurzydłowski, K. J. Titanium-Related Color Centers in Diamond: a Density Functional Theory Prediction. *J. Mater. Chem. C* **2018**, *6*, 5261–5268.

(2) Deng, B.; Zhang, R. Q.; Shi, X. Q. New Insight into the Spin-Conserving Excitation of the Negatively Charged Nitrogen-Vacancy Center in Diamond. *Sci. Rep.* **2014**, *4*, 5144.

(3) Ekimov, E. A.; Sherin, P. S.; Krivobok, V. S.; Lyapin, S. G.; Gavva, V. A.; Kondrin, M. V. Photoluminescence Excitation Study of Split-Vacancy Centers in Diamond. *Phys. Rev. B* **2018**, *97*, 045206.

(4) El-Ella, H. A. R. Magnon Condensation in a Dense Nitrogen-Vacancy Spin Ensemble. *Phys. Rev. B* **2019**, *99*, 024414.

(5) Li, Z.; Chen, Y.; Jian, Z.; Jiang, H.; Razink, J. J.; Stickle, W. F.; Neuefeind, J. C.;

Ji, X. Defective Hard Carbon Anode for Na-Ion Batteries. *Chem. Mater.* **2018**, *30*, 4536–4542.

(6) Schirhagl, R.; Chang, K.; Loretz, M.; Degen, C. L. Nitrogen-Vacancy Centers in Diamond: Nanoscale Sensors for Physics and Biology. *Annu. Rev. Phys. Chem.* **2014**, *65*, 83–105.

(7) Slepetz, B.; Kertesz, M. Divacancies in Diamond: a Stepwise Formation Mechanism. *Phys. Chem. Chem. Phys.* **2014**, *16*, 1515–1521.

(8) Thiering, G.; Gali, A. Characterization of Oxygen Defects in Diamond by Means of Density Functional Theory Calculations. *Phys. Rev. B* **2016**, *94*, 125202.

(9) Vanpoucke, D. E. P.; Haenen, K. Revisiting the Neutral C-Vacancy in Diamond: Localization of Electrons through DFT+U. *Diamond Relat. Mater.* **2017**, *79*, 60–69.

(10) Zhang, J.; Wang, C.-Z.; Zhu, Z.; Liu, Q. H.; Ho, K.-M. Multimode Jahn-Teller Effect in Bulk Systems: a Case of the NV^0 Center in Diamond. *Phys. Rev. B* **2018**, *97*, 165204.

(11) Childress, L.; Dutt, M. V. G.; Taylor, J. M.; Zibrov, A. S.; Jelezko, F.; Wrachtrup, J.; Hemmer, P. R.; Lukin, M. D. Coherent Dynamics of Coupled Electron and Nuclear Spin Qubits in Diamond. *Science* **2006**, *314*, 281–285.

(12) Maurer, P. C.; Kucsko, G.; Latta, C.; Jiang, L.; Yao, N. Y.; Bennett, S. D.; Pastawski, F.; Hunger, D.; Chisholm, N.; Markham, M.; Twitchen, D. J.; Cirac, J. I.; Lukin, M. D. Room-Temperature Quantum Bit Memory Exceeding One Second. *Science* **2012**, *336*, 1283–1286.

(13) Yao, N. Y.; Jiang, L.; Gorshkov, A. V.; Gong, Z.-X.; Zhai, A.; Duan, L.-M.; Lukin, M. D. Robust Quantum State Transfer in Random Unpolarized Spin Chains. *Phy. Rev. Lett.* **2011**, *106*, 040505.

(14) Yao, N. Y.; Jiang, L.; Gorshkov, A. V.; Maurer, P. C.; Giedke, G.; Cirac, J. I.; Lukin, M. D. Scalable Architecture for a Room Temperature Solid-State Quantum Information Processor. *Nat. Commun.* **2012**, *3*, 800.

(15) Kucsko, G.; Maurer, P. C.; Yao, N. Y.; Kubo, M.; Noh, H. J.; Lo, P. K.; Park, H.; Lukin, M. D. Nanometre-Scale Thermometry in a Living Cell. *Nature* **2013**, *500*, 54–58.

(16) Lovchinsky, I.; Sushkov, A. O.; Urbach, E.; de Leon, N. P.; Choi, S.; De Greve, K.; Evans, R.; Gertner, R.; Bersin, E.; Müller, C.; McGuinness, L.; Jelezko, F.; Walsworth, R. L.; Park, H.; Lukin, M. D. Nuclear Magnetic Resonance Detection and Spectroscopy of Single Proteins Using Quantum Logic. *Science* **2016**, *351*, 836–841.

(17) Mamin, H. J.; Kim, M.; Sherwood, M. H.; Rettner, C. T.; Ohno, K.; Awschalom, D. D.; Rugar, D. Nanoscale Nuclear Magnetic Resonance with a Nitrogen-Vacancy Spin Sensor. *Science* **2013**, *339*, 557–560.

(18) Maurer, P. C.; Maze, J. R.; Stanwix, P. L.; Jiang, L.; Gorshkov, A. V.; Zibrov, A. A.; Harke, B.; Hodges, J. S.; Zibrov, A. S.; Yacoby, A.; Twitchen, D.; Hell, S. W.; Walsworth, R. L.; Lukin, M. D. Far-Field Optical Imaging and Manipulation of Individual Spins with Nanoscale Resolution. *Nat. Phys.* **2010**, *6*, 912–918.

(19) Morita, M.; Tachikawa, T.; Seino, S.; Tanaka, K.; Majima, T. Controlled Synthesis of Gold Nanoparticles on Fluorescent Nanodiamond via Electron-Beam-Induced Reduction Method for Dual-Modal Optical and Electron Bioimaging. *ACS Appl. Nano Mater.* **2018**, *1*, 355–363.

(20) Chen, L.; Miao, X.; Ma, H.; Guo, L.; Wang, Z.; Yang, Z.; Fang, C.; Jia, X. Synthesis and Characterization of Diamonds with Different Nitrogen Concentrations under High Pressure and High Temperature Conditions. *CrystEngComm* **2018**, *20*, 7164–7169.

(21) Dhomkar, S.; Jayakumar, H.; Zangara, P. R.; Meriles, C. A. Charge Dynamics in Near-Surface, Variable-Density Ensembles of Nitrogen-Vacancy Centers in Diamond. *Nano Lett.* **2018**, *18*, 4046–4052.

(22) Jarmola, A.; Berzins, A.; Smits, J.; Smits, K.; Prikulis, J.; Gahbauer, F.; Ferber, R.; Erts, D.; Auzinsh, M.; Budker, D. Longitudinal Spin-Relaxation in Nitrogen-Vacancy Centers in Electron Irradiated Diamond. *Appl. Phys. Lett.* **2015**, *107*, 242403.

(23) Kucsko, G.; Choi, S.; Choi, J.; Maurer, P. C.; Zhou, H.; Landig, R.; Sumiya, H.; Onoda, S.; Isoya, J.; Jelezko, F.; Demler, E.; Yao, N. Y.; Lukin, M. D. Critical Thermalization of a Disordered Dipolar Spin System in Diamond. *Phys. Rev. Lett.* **2018**, *121*, 023601.

(24) Liu, C.; Dutt, M. V. G.; Pekker, D. Single-Photon Heralded Two-Qubit Unitary Gates for Pairs of Nitrogen-Vacancy Centers in Diamond. *Phys. Rev. A* **2018**, *98*, 052342.

(25) Mrózek, M.; Rudnicki, D.; Kehayias, P.; Jarmola, A.; Budker, D.; Gawlik, W. Longitudinal Spin Relaxation in Nitrogen-Vacancy Ensembles in Diamond. *EPJ Quantum Technol.* **2015**, *2*, 22.

(26) Pfaff, W.; Hensen, B. J.; Bernien, H.; van Dam, S. B.; Blok, M. S.; Taminiau, T. H.; Tiggelman, M. J.; Schouten, R. N.; Markham, M.; Twitchen, D. J.; Hanson, R. Unconditional Quantum Teleportation between Distant Solid-State Quantum Bits. *Science* **2014**, *345*, 532–535.

(27) Kleinsasser, E. E.; Stanfield, M. M.; Banks, J. K. Q.; Zhu, Z.; Li, W.-D.; Acosta, V. M.; Watanabe, H.; Itoh, K. M.; Fu, K.-M. C. High Density Nitrogen-Vacancy Sensing Surface Created via He^+ Ion Implantation of ^{12}C Diamond. *Appl. Phys. Lett.* **2016**, *108*, 202401.

(28) Pezzagna, S.; Rogalla, D.; Wildanger, D.; Meijer, J.; Zaitsev, A. Creation and Na-

ture of Optical Centres in Diamond for Single-Photon Emission-Overview and Critical Remarks. *New J. Phys.* **2011**, *13*, 035024.

(29) Schröder, T.; Walsh, M.; Zheng, J.; Mouradian, S.; Li, L.; Malladi, G.; Bakhru, H.; Lu, M.; Stein, A.; Heuck, M.; Englund, D. Scalable Fabrication of Coupled NV Center - Photonic Crystal Cavity Systems by Self-Aligned N Ion Implantation. *Opt. Mater. Express* **2017**, *7*, 1514–1524.

(30) van Dam, S. B.; Walsh, M.; Degen, M. J.; Bersin, E.; Mouradian, S. L.; Galiullin, A.; Ruf, M.; IJspeert, M.; Taminiau, T. H.; Hanson, R.; Englund, D. R. Optical Coherence of Diamond Nitrogen-Vacancy Centers Formed by Ion Implantation and Annealing. *Phys. Rev. B* **2019**, *99*, 161203.

(31) Choi, J.; Choi, S.; Kucsko, G.; Maurer, P. C.; Shields, B. J.; Sumiya, H.; Onoda, S.; Isoya, J.; Demler, E.; Jelezko, F.; Yao, N. Y.; Lukin, M. D. Depolarization Dynamics in a Strongly Interacting Solid-State Spin Ensemble. *Phys. Rev. Lett.* **2017**, *118*, 093601.

(32) Chou, J.-P.; Bodrog, Z.; Gali, A. First-Principles Study of Charge Diffusion between Proximate Solid-State Qubits and Its Implications on Sensor Applications. *Phys. Rev. Lett.* **2018**, *120*, 136401.

(33) Manson, N. B.; Hedges, M.; Barson, M. S. J.; Ahlefeldt, R.; Doherty, M. W.; Abe, H.; Ohshima, T.; Sellars, M. J. NV^--N^+ Pair Centre in 1b Diamond. *New J. Phys.* **2018**, *20*, 113037.

(34) Kobayashi, Y.; Nishimura, T.; Yamaguchi, H.; Tamai, N. Effect of Surface Defects on Auger Recombination in Colloidal CdS Quantum Dots. *J. Phys. Chem. Lett.* **2011**, *2*, 1051–1055.

(35) Kobayashi, Y.; Pan, L.; Tamai, N. Effects of Size and Capping Reagents on Biexciton Auger Recombination Dynamics of CdTe Quantum Dots. *J. Phys. Chem. C* **2009**, *113*, 11783–11789.

(36) Kobayashi, Y.; Udagawa, T.; Tamai, N. Carrier Multiplication in CdTe Quantum Dots by Single-Photon Timing Spectroscopy. *Chem. Lett.* **2009**, *38*, 830–831.

(37) Kim, D.; Okahara, S.; Nakayama, M.; Shim, Y. Experimental Verification of Förster Energy Transfer between Semiconductor Quantum Dots. *Phys. Rev. B* **2008**, *78*, 153301.

(38) Gali, A.; Fyta, M.; Kaxiras, E. Ab Initio Supercell Calculations on Nitrogen-Vacancy Center in Diamond: Electronic Structure and Hyperfine Tensors. *Phys. Rev. B* **2008**, *77*, 155206.

(39) Rand, S. C.; Lenef, A.; Brown, S. W. Zeeman Coherence and Quantum Beats in Ultrafast Photon Echoes of N-V Centers in Diamond. *J. Lumin.* **1994**, *60-61*, 739–741.

(40) Rhee, H.; June, Y.-G.; Lee, J.-S.; Lee, K.-K.; Ha, J.-H.; Kim, Z.-H.; Jeon, S.-J.; Cho, M. Femtosecond Characterization of Vibrational Optical Activity of Chiral Molecules. *Nature* **2009**, *458*, 310–313.

(41) Sato, M.; Kumada, A.; Hidaka, K.; Hirano, T.; Sato, F. Computational Study on Hole Conduction in Normal Alkanes: Anisotropy and Effect of Dynamic Disorder. *Appl. Phys. Lett.* **2017**, *110*, 092903.

(42) Ulbricht, R.; Dong, S.; Chang, I.-Y.; Mariserla, B. M. K.; Dani, K. M.; Hyeon-Deuk, K.; Loh, Z.-H. Jahn-Teller-Induced Femtosecond Electronic Depolarization Dynamics of the Nitrogen-Vacancy Defect in Diamond. *Nat. Commun.* **2016**, *7*, 13510.

(43) Ulbricht, R.; Dong, S.; Gali, A.; Meng, S.; Loh, Z.-H. Vibrational Relaxation Dynamics of the Nitrogen-Vacancy Center in Diamond. *Phys. Rev. B* **2018**, *97*, 220302.

(44) Ulbricht, R.; Loh, Z.-H. Excited-State Lifetime of the NV^- Infrared Transition in Diamond. *Phys. Rev. B* **2018**, *98*, 094309.

(45) Zhang, J.; Wang, C.-Z.; Zhu, Z. Z.; Dobrovitski, V. V. Vibrational Modes and Lattice

Distortion of a Nitrogen-Vacancy Center in Diamond from First-Principles Calculations. *Phys. Rev. B* **2011**, *84*, 035211.

(46) Kim, D.; Mishima, T.; Tomihira, K.; ; Nakayama, M. Temperature Dependence of Photoluminescence Dynamics in Colloidal CdS Quantum Dots. *J. Phys. Chem. C* **2008**, *112*, 10668-10673.

(47) Kim, D.; Okazaki, K.; Nakayama, M. Temperature Dependence of the Energy Transfer of Exciton States in Bilayer Structures of CdSe/ZnS Quantum Dots. *Phys. Rev. B* **2009**, *80*, 045322.

(48) Huxter, V. M.; Oliver, T. A. A.; Budker, D.; Fleming, G. R. Vibrational and Electronic Dynamics of Nitrogen-Vacancy Centres in Diamond Revealed by Two-Dimensional Ultrafast Spectroscopy. *Nat. Phys.* **2013**, *9*, 744–749.

(49) Konzelmann, P.; Rendler, T.; Bergholm, V.; Zappe, A.; Pfannenstill, V.; Garsi, M.; Ziem, F.; Niethammer, M.; Widmann, M.; Lee, S.-Y.; Neumann, P.; Wrachtrup, J. Robust and Efficient Quantum Optimal Control of Spin Probes in a Complex (Biological) Environment. Towards Sensing of Fast Temperature Fluctuations. *New J. Phys.* **2018**, *20*, 123013.

(50) Thiering, G.; Gali, A. Theory of the Optical Spin-Polarization Loop of the Nitrogen-Vacancy Center in Diamond. *Phys. Rev. B* **2018**, *98*, 085207.

(51) Collins, A. T.; Stanley, M.; Woods, G. S. Nitrogen Isotope Effects in Synthetic Diamonds. *J. Phys. D: Appl. Phys.* **1987**, *20*, 969–974.

(52) Davies, G.; Hamer, M. F. Optical Studies of 1.945 eV Vibronic Band in Diamond. *Proc. R. Soc. A* **1976**, *348*, 285–298.

(53) Zaitsev, A. M. Vibronic Spectra of Impurity-Related Optical Centers in Diamond. *Phys. Rev. B* **2000**, *61*, 12909–12922.

(54) Alkauskas, A.; McCluskey, M. D.; Van de Walle, C. G. Tutorial: Defects in Semiconductors—Combining Experiment and Theory. *J. Appl. Phys.* **2016**, *119*, 181101.

(55) Goldman, M. L.; Doherty, M. W.; Sipahigil, A.; Yao, N. Y.; Bennett, S. D.; Manson, N. B.; Kubanek, A.; Lukin, M. D. State-Selective Intersystem Crossing in Nitrogen-Vacancy Centers. *Phys. Rev. B* **2015**, *91*, 165201.

(56) Goldman, M. L.; Sipahigil, A.; Doherty, M. W.; Yao, N. Y.; Bennett, S. D.; Markham, M.; Twitchen, D. J.; Manson, N. B.; Kubanek, A.; Lukin, M. D. Phonon-Induced Population Dynamics and Intersystem Crossing in Nitrogen-Vacancy Centers. *Phys. Rev. Lett.* **2015**, *114*, 145502.

(57) Plakhotnik, T.; Doherty, M. W.; Manson, N. B. Electron-Phonon Processes of the Nitrogen-Vacancy Center in Diamond. *Phys. Rev. B* **2015**, *92*, 081203.

(58) Manson, N. B.; McMurtrie, R. L. Issues Concerning the Nitrogen-Vacancy Center in Diamond. *J. Lumin.* **2007**, *127*, 98–103.

(59) Chang, I.-Y.; Kim, D.; Hyeon-Deuk, K. Control of Electronic Structures and Phonon Dynamics in Quantum Dot Superlattices by Manipulation of Interior Nanospace. *ACS Appl. Mater. Interfaces* **2016**, *8*, 18321–18327.

(60) Hyeon-Deuk, K.; Kim, J.; Prezhdo, O. V. Ab Initio Analysis of Auger-Assisted Electron Transfer. *J. Phys. Chem. Lett.* **2015**, *6*, 244–249.

(61) Hyeon-Deuk, K.; Kobayashi, Y.; Tamai, N. Evidence of Phonon-Assisted Auger Recombination and Multiple Exciton Generation in Semiconductor Quantum Dots Revealed by Temperature-Dependent Phonon Dynamics. *J. Phys. Chem. Lett.* **2014**, *5*, 99–105.

(62) Hyeon-Deuk, K.; Madrid, A. B.; Prezhdo, O. V. Symmetric Band Structures and Asym-

metric Ultrafast Electron and Hole Relaxations in Silicon and Germanium Quantum Dots: Time-Domain Ab Initio Simulation. *Dalton Trans.* **2009**, *45*, 10069–10077.

(63) Hyeon-Deuk, K.; Prezhdo, O. V. Time-Domain Ab Initio Study of Auger and Phonon-Assisted Auger Processes in a Semiconductor Quantum Dot. *Nano Lett.* **2011**, *11*, 1845–1850.

(64) Hyeon-Deuk, K.; Prezhdo, O. V. Multiple Exciton Generation and Recombination Dynamics in Small Si and CdSe Quantum Dots: an Ab Initio Time-Domain Study. *ACS Nano* **2012**, *6*, 1239–1250.

(65) Hyeon-Deuk, K.; Prezhdo, O. V. Photoexcited Electron and Hole Dynamics in Semiconductor Quantum Dots: Phonon-Induced Relaxation, Dephasing, Multiple Exciton Generation and Recombination. *J. Phys. : Condens. Matter* **2012**, *24*, 363201.

Supporting Information for " Ultrafast Orbital Depolarization and Defect-Localized Phonon Dynamics Induced by Quantum Resonance between Multi-Nitrogen Vacancy Defects"

I-Ya Chang and Kim Hyeon-Deuk*

Department of Chemistry, Kyoto University, Kyoto, 606-8502, Japan

* Spokesperson: kim@kuchem.kyoto-u.ac.jp

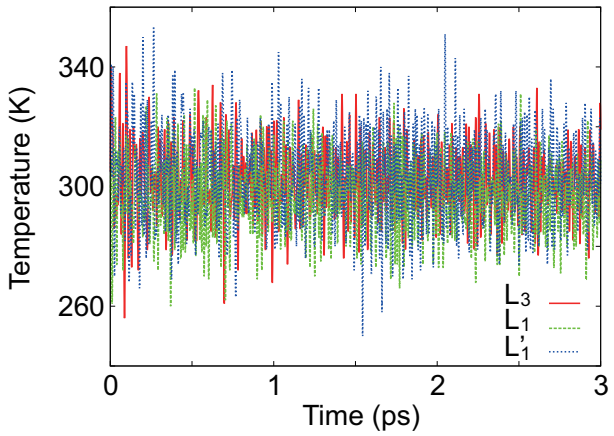

Figure S1: Temperature fluctuations in the excited-state (ES) ab initio molecular dynamics (AIMD) simulations of L_3, L_1 and L'_1 as a function of time. The temperature fluctuations exhibit little difference among the three cases: The temperature averages are 301.8 K, 297.0 K, and 303.8 K while their standard deviations are 11.5 K, 11.7 K, and 14.8 K for L_3, L_1 and L'_1, respectively. The current stable temperature fluctuations would not be realized if the structures were unstable or fragile.

Atom	L_3 (GS)	L_1 (GS)	L'_1 (GS)	L_3 (300 K)	L_1 (300 K)	L'_1 (300 K)
N	0.009	0.028	0.017	0.001	0.000	0.000
C	0.004	0.030	0.034	0.001	0.000	0.000
C	0.014	0.036	0.038	0.000	0.000	0.000
C	0.006	0.030	0.034	0.001	0.000	0.000
N	0.059	0.062	0.016	0.001	0.000	0.000
C	0.050	0.038	0.033	0.001	0.000	0.000
C	0.067	0.050	0.038	0.001	0.000	0.000
C	0.066	0.039	0.034	0.001	0.000	0.000
RMSD	0.043	0.041	0.032	0.001	0.000	0.000

Table S1: Root-square displacements (RSDs) of the two N atoms and six C atoms around the two vacancy defects between the ground state (GS) and the excited state (ES) at 0 K, and the RSDs between the averaged ES at 300 K and the ES at 0 K. The unit is Å. The RSDs between the GS and the ES at 0 K reflect the Jahn-Teller (JT) distortion induced by the electron excitation from the orbital 1020 to the orbital 1021. In L_3 and L_1, the RSDs of the two nitrogen-vacancy (NV) defects are asymmetric; the RSDs of the first NV defect is totally smaller than the RSDs of the second NV defect. This is due to the asymmetric deformation of the occupied defect orbitals around the two NV defects upon the electron excitation. (Compare the orbitals 1019 and 1020 in the GS at 0 K and the orbitals 1019 and 1021 in the ES at 0 K drawn in Figs.S4 and S5.) As shown in Fig.S6, L'_1 has the occupied defect orbitals symmetrically existing around the two NV defects both on the GS and ES at 0 K, leading to the almost symmetric RSDs of the first and second NV defects in the L'_1 case. As the root-mean-square displacements (RMSDs) demonstrate, the average structural

disorder between the GS and the ES at 0 K is larger in L_3 than in L_1 and L'_1, indicating that the L_3 structure is more flexible due to more C atoms aligned between the two NV defects. The average thermal disorder on the ES at 300 K is quite small in all the cases reflecting stable structure modulations around the optimized ES structure at 0 K.

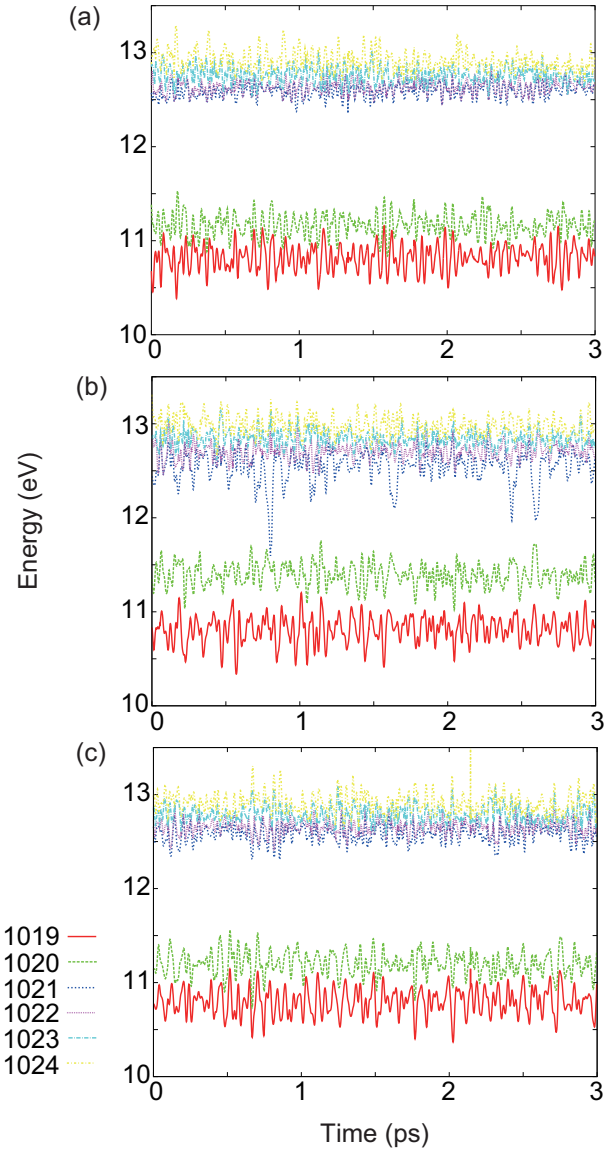

Figure S2: Real-time absolute defect orbital energies of (a) L_3, (b) L_1 and (c) L'_1 on the ES at 300 K. The instantaneous orbital energies at 1 ps, 2 ps and 3 ps and the averaged orbital energies over 3 ps were taken from the above time-dependent orbital energies and given in Table S2 and Fig.2, respectively. The lower-energy orbitals 1019 and 1020 have the most significantly fluctuating energies among the NV defect orbitals. This is because the orbitals 1019 and 1020 spread over all the defect core atoms which are adjacent to the vacancy defects and have the most flexible structure and atomic motions. The larger energy

fluctuations of the orbitals 1019 and 1020 result in their enhanced intensity of the phonon modes as shown in Figs.3(a) and 3(b). In contrast, the time-dependent energies of the orbitals 1022-1024 fluctuate moderately and are more degenerate even at 300 K compared to the two lower-energy orbitals.

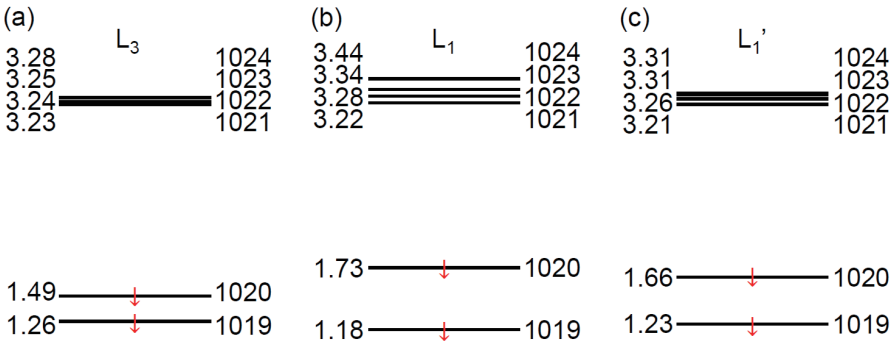

Figure S3: Defect orbital energies relative to the highest energy of the valence band (VB) orbitals of (a) L_3, (b) L_1 and (c) L'_1 optimized on the GS at 0 K. The unit is eV.

	L_3			L_1			L'_1		
Orbital Number	1 ps	2 ps	3 ps	1 ps	2 ps	3 ps	1 ps	2 ps	3 ps
1019	10.97	10.75	10.82	10.88	10.79	10.84	10.83	11.05	11.03
1020	11.17	11.22	11.24	11.39	11.37	11.30	11.23	11.37	11.37
1021	12.64	12.59	12.64	12.59	12.54	12.65	12.67	12.68	12.53
1022	12.69	12.61	12.64	12.63	12.62	12.69	12.71	12.72	12.66
1023	12.85	12.68	12.67	12.92	12.81	12.83	12.74	12.77	12.68
1024	13.15	12.80	13.00	12.93	12.86	12.94	12.79	12.80	12.78

Table S2: Instantaneous absolute defect orbital energies of L_3, L_1 and L'_1 at 1 ps, 2 ps and 3 ps during the ES AIMD simulations. The unit is eV. The instantaneous energies correspond to the defect orbitals drawn in Figs.S4-S6. These numerical data were taken from Fig.S2. The defect orbital energies largely fluctuate at 300 K depending on time, supporting the time-dependent altering orbitals demonstrated in Figs.S4-S6.

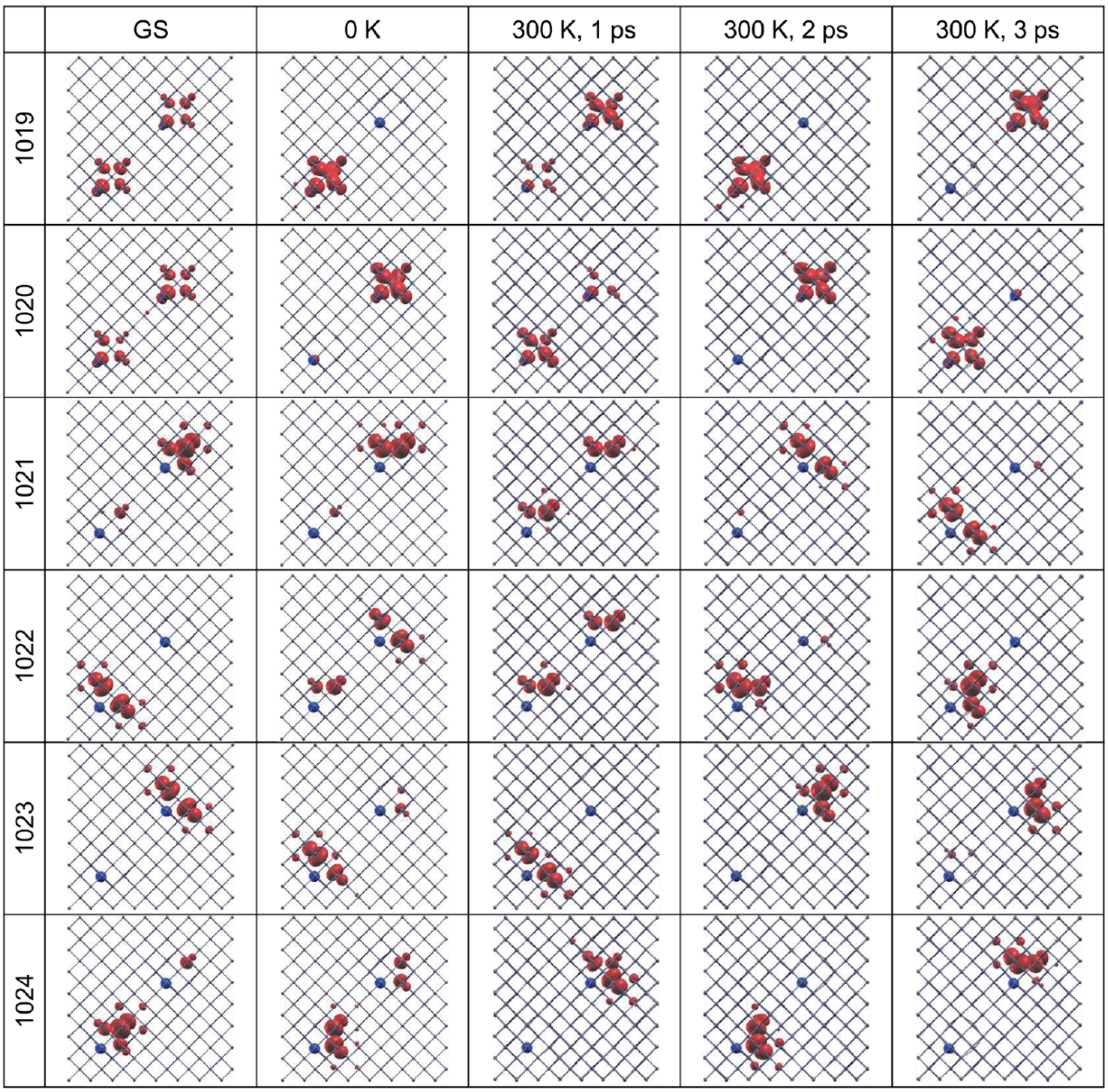

Figure S4: Optimized defect orbitals of L_3 on the GS and ES at 0 K, and time-dependent defect orbitals of L_3 at 1 ps, 2 ps and 3 ps in the ES AIMD simulations at 300 K. The orbitals 1021 and 1020 are extracted and shown in Figs.2(d) and 2(e). The orbital energies are listed in Table S2 and in Fig.2(a)-2(c). The lower-energy orbitals 1019 and 1020 on the GS at 0 K exist simultaneously at both of the two NV defects. This however disappears on the ES at 0 K because of the JT distortion.

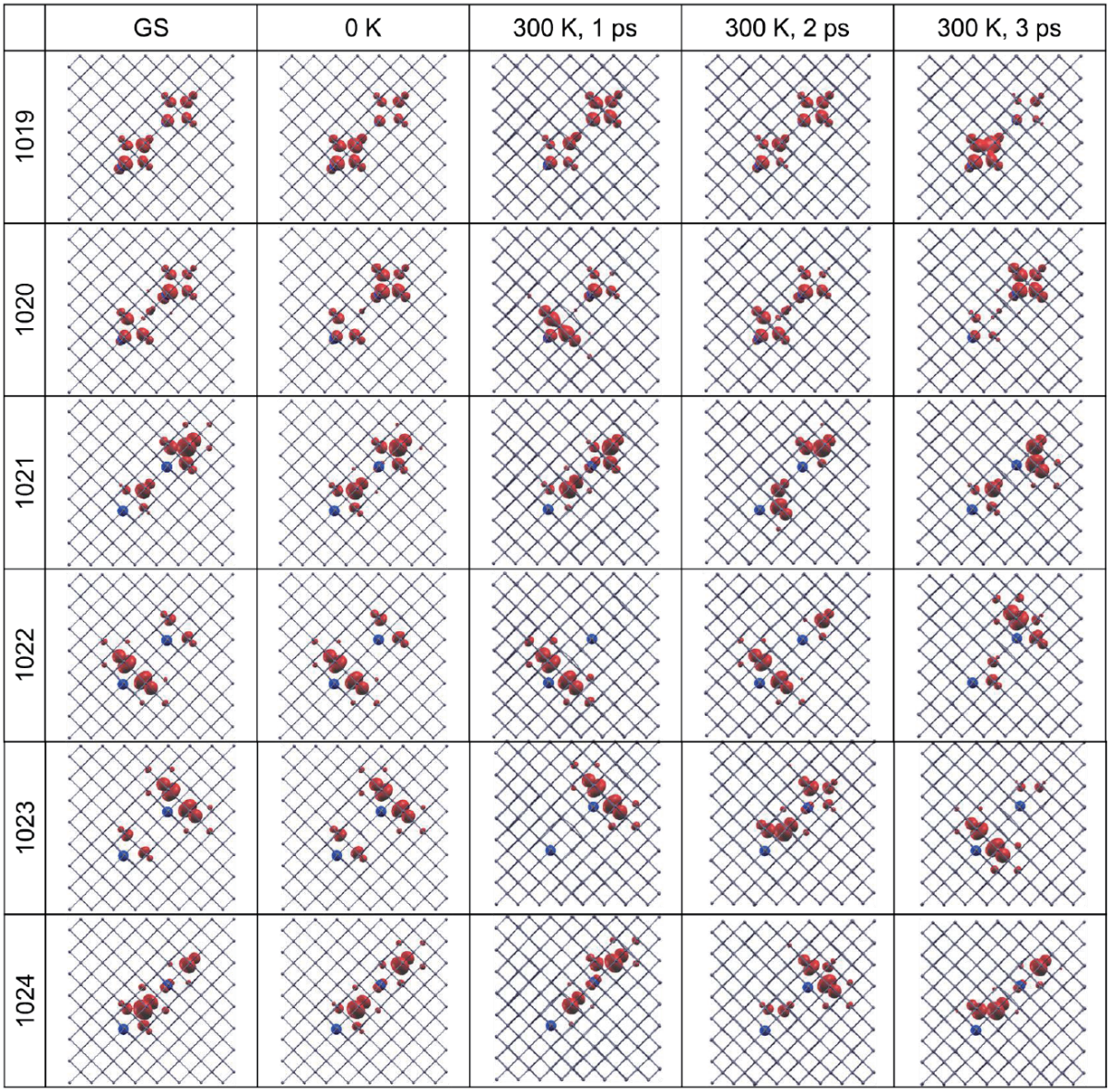

Figure S5: Same as Fig.S4 but for L_1.

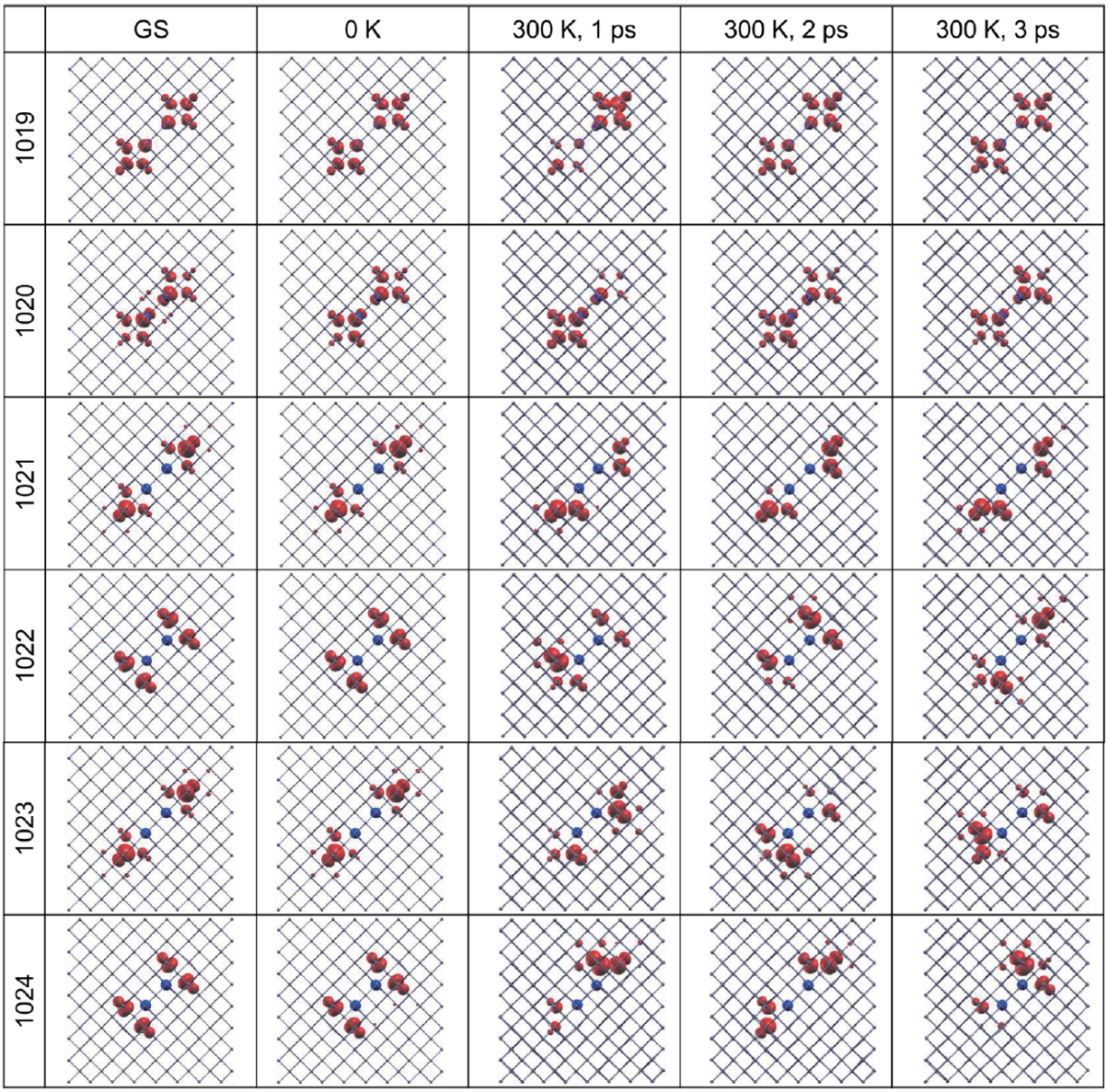

Figure S6: Same as Fig.S4 but for L'$_1$. The lower-energy orbitals 1019 and 1020 stably keeps their lobe shape, which is similar to the L_1 case while different from the L_3 case.

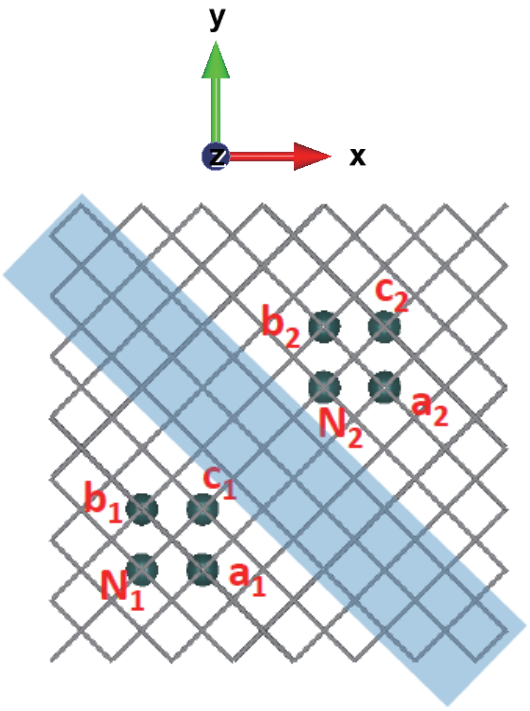

Figure S7. Structure of periodic diamond cell which includes two NV defects. The locations of the four core atoms, one N atom and three C atoms, are labeled as N_1, a_1, b_1 and c_1 for the first NV defect and N_2, a_2, b_2 and c_2 for the second NV defect, respectively. The blue-shadowed area denotes the spacing C-atom layers between the two NV defects in the periodic diamond cell.

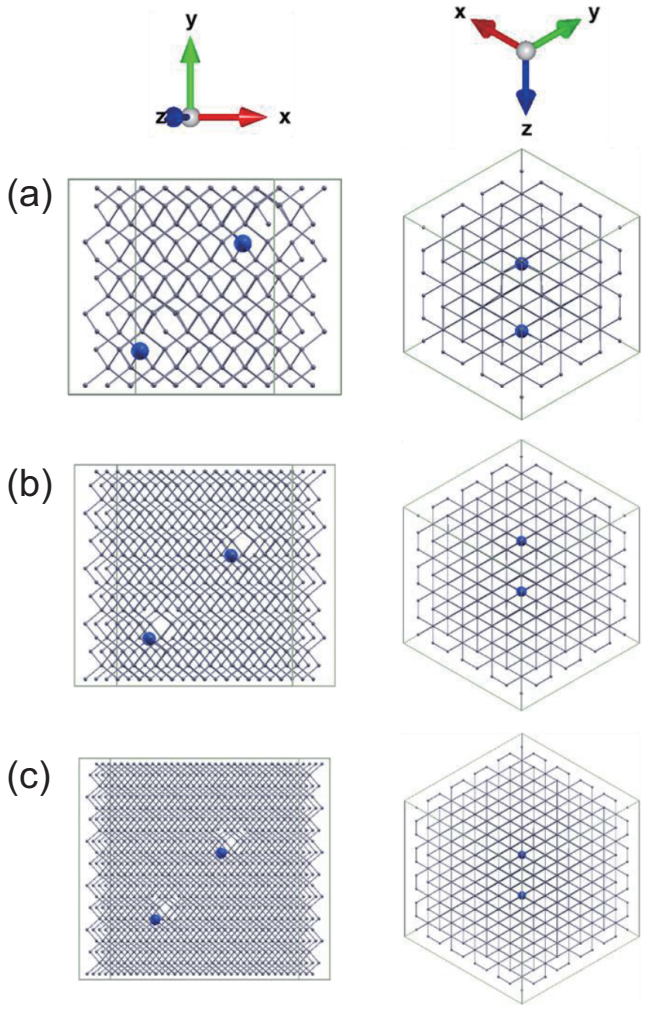

Figure S8: Three L_3 configurations of different cell size composed of (a) $C_{212}N_2$ (10.7 Å × 10.7 Å × 10.7 Å), (b) $C_{508}N_2$ (14.3 Å × 14.3 Å × 14.3 Å) and (c) $C_{996}N_2$ (17.8 Å × 17.8 Å × 17.8 Å).

$C_{212}N_2$	$C_{508}N_2$	$C_{996}N_2$	Difference
1.265	1.260	1.341	-0.081
1.491	1.492	1.558	-0.066
2.902	3.232	3.293	-0.061
3.265	3.245	3.297	-0.052
3.279	3.252	3.336	-0.084
3.605	3.288	3.365	-0.077

Table S3: Defect orbital energies relative to the highest energy of the VB orbitals in the three L_3 configurations drawn in Fig.S8. The unit is eV. The far right column lists the orbital energy difference between $C_{508}N_2$ and $C_{996}N_2$.

Orbital Number	Dispersion Correction (DFT-D3)	No Correction	Difference
1019	1.255	1.260	-0.005
1020	1.487	1.490	-0.003
1021	3.233	3.229	0.004
1022	3.245	3.241	0.004
1023	3.252	3.248	0.004
1024	3.289	3.285	0.004

Table S4: Defect orbital energies relative to the highest energy of the VB orbitals of L_3 calculated with and without the dispersion correction. The unit is eV.

Orbital Number	Dispersion Correction (DFT-D3)	No Correction	Difference
1019	1.174	1.180	-0.006
1020	1.730	1.732	-0.002
1021	3.225	3.221	0.004
1022	3.280	3.275	0.005
1023	3.343	3.338	0.005
1024	3.443	3.437	0.006

Table S5: Same as Table S4 but for L_1.

Lattice Vector	L_3			L_1			L'_1		
a	14.29	0.00	0.00	14.29	0.00	0.00	14.29	0.00	0.00
b	0.00	14.29	0.00	0.00	14.29	0.00	0.00	14.29	0.00
c	0.00	0.00	14.29	0.00	0.00	14.30	0.00	0.00	14.30

Table S6: Lattice parameters of L_3, L_1 and L'_1 freely optimized on the ES at 0 K. The unit is Å.

	GS			ES		
Orbital Number	HSE06	PBE	Difference	HSE06	PBE	Difference
1019	0.00	0.00	-	0.00	0.00	-
1020	0.55	0.55	0.00	0.93	0.50	0.43
1021	2.99	2.04	0.95	2.09	1.76	0.33
1022	3.03	2.10	0.93	2.63	1.92	0.71
1023	3.12	2.16	0.96	2.76	1.98	0.78
1024	3.22	2.26	0.96	2.86	2.04	0.82

Table S7: Comparison of the defect orbital energies relative to the 1019 orbital energy of L_1 on the GS and ES at 0 K obtained with the Heyd-Scuseria-Ernzerhof (HSE) 06 and Perdew, Burke and Ernzerhof (PBE) functionals. The difference between the orbital energies obtained with the HSE06 and PBE functionals is systematic; the HSE06 functional increases the energies of the unoccupied orbitals while it decreases the energies of the occupied orbitals. In fact, as seen in the fourth column, the energy difference in the unoccupied orbitals 1021-1024 on the GS becomes uniform, approximately 0.95 eV. The energy difference in the ES is slightly more complicated because the originally occupied orbital 1020 is now unoccupied and the originally unoccupied orbital 1021 is now occupied, which is implied by the fact that the sum of the energy changes in the orbitals 1020 and 1021, 0.76 eV, is close to the other energy changes in the higher-energy orbitals 1022-1024. (See the seventh column)

Computational Methods

Structure design : The primitive structure is a periodic cubic supercell of a diamond crystal structure containing 512 C atoms. The length of the periodic cubic cell is 14.3 Å at each side. The NV diamond cell which contains the two NV defects was built by removing two C atoms from the primitive cubic supercell and replace one of the C atoms closest to each removed C location by an N atom at each defect site. As a result, each NV defect was composed of one vacancy site and four closest atoms, one N atom and three C atoms as shown in Fig.S7. The total charge of the designed NV diamond cell was set to be -2. The notation of the system L_3 means that there are three spacing C-atom layers between the two NV defects.(Fig.S7) The notations of the other systems L_1 and L'_1 mean that there is only one spacing C-atom layer between the two NV defects. Note that, in L'_1, N_1 and c_1 were exchanged as shown in Fig.1. In order to check the finite size effects of the periodic NV diamond cell, we additionally introduced the two different-sized cells for L_3: $C_{212}N_2$ (10.7 Å × 10.7 Å × 10.7 Å) and $C_{996}N_2$ (17.8 Å × 17.8 Å × 17.8 Å). (See Fig.S8) L_3 has the largest distance between the two NV defects and should be affected more by the finite system size.

Structure and energy on the GS at 0 K : All the following ab initio calculations were performed by Vienna Ab-initio Simulation Package (VASP). [1] Unless otherwise stated, structures and energies were computed by generalized-gradient approximation and projector-augmented-wave pseudopotentials of the PBE functional with the 420 eV energy cutoff for the plan-wave basis set. We applied the Γ-point to map the Brillouin-zone. For checking the finite size effects of the periodic NV diamond cell, we calculated and compared the defect orbital energies in the above three different cells for L_3. The C_{1h}-symmetry was constrained and the cell size was frozen in these three structural optimizations while no occupation restriction was set. We confirmed that all the defect orbital energies are uniformly upper-

shifted in $C_{996}N_2$ compared to $C_{508}N_2$ by the order of 10^{-2} eV which is irrelevant to the current discussions and conclusions. (See Table S3) Thus, $C_{508}N_2$ was chosen in all the following calculations including the AIMD simulations at 300 K. The further GS structures and cell sizes of $C_{508}N_2$ at 0 K were calculated without any geometrical and occupation constraints. We also examined the role of the long-range dispersion force which could stem from the long-range dipole-dipole interaction between the two NV defects. The dispersion correction was taken into account by the DFT-D3 method embedded in VASP. Tables S4 and S5 show the defect orbital energies of L_3 and L_1 calculated with and without the dispersion correction. The difference appears in the order of 10^{-3} eV in the both cases, meaning that the long-range dispersion interaction between the two NV defects can be neglected. The structural change due to the inclusion of the dispersion correction, defined as the RMSD, is only 0.015 Å and also negligible. The relative total energy of L_1 to L_3 is the same, 0.13 eV, regardless of the existence of the dispersion correction.

Structure and energy on the ES at 0 K : As shown in Fig.2, the defect orbitals involved in the present photoexcitation and non-adiabatic (NA) dynamics of the multi-NV defects are the orbitals from 1019 to 1024. The orbital 1018 corresponds to the highest-energy orbital of the VB while the orbital 1025 is the lowest-energy orbital of the conduction band. Thus, the electronic configuration of the two NV defects on the first ES of quintet is $(1019)^{\uparrow\downarrow}(1020)^{\uparrow}(1021)^{\uparrow\downarrow}(1022)^{\uparrow}(1023)^{\uparrow}(1024)^{\uparrow}$. All the structures and cell sizes on the ES at 0 K were freely optimized under this electronic configuration. (See Table S6) For the optimized ES structure of L_1 which exhibits the stronger quantum resonance, single-point calculations were further performed with the HSE06 functional with the same plane-wave basis set. Table S7 compares the defect orbital energies on the ES obtained with the HSE06 and PBE functionals. We emphasize that the PBE defect orbital energies can still keep the

most important properties to elucidate the current ES NA transition dynamics among the defect orbitals: (1) the three largest energy gaps appear in the same order; the largest gap appears between the orbitals 1021 and 1020, the second largest gap appears between the orbitals 1020 and 1019, and the third largest gap appears between the orbitals 1022 and 1021. (2) The three orbitals 1022-1024 form a relatively degenerate band and they are energetically close. Therefore, the current NA transition dynamics should be at least semiquantitatively correct as was demonstrated in the single NV defect case[2], and the above deviations between the HSE06 and PBE functionals are irrelevant to the suggested physical insights and conclusions on the depolarization dynamics and phonon modes in this study. Actually, the PBE functional has been widely adopted in many defect cases including structures[3–6], energies[3, 7, 8] and phonon modes[4, 6, 9]. Balancing the computational cost and accuracy, we chose the PBE functional to semiquantitatively describe the NA transition dynamics among the defect orbitals at the ambient temperature. We also emphasize that the ambient temperature inducing the thermal modulations of the orbital energies shown in Fig.S2 and the orbital altering shown in Figs.S4-S6 rather plays a pivotal role to determine the current depolarization dynamics and phonon modes.

AIMD simulations at 300 K : The ES structures of L_3, L_1 and L'_1 optimized at 0 K were heated up to 300 K by repeated velocity rescaling under the same electronic occupation $(1019)^{\uparrow\downarrow}(1020)^{\uparrow}(1021)^{\uparrow\downarrow}(1022)^{\uparrow}(1023)^{\uparrow}$ $(1024)^{\uparrow}$. After the careful equilibration, microcanonical MD trajectories of 3 ps were produced on the ES using the Verlet algorithm with a 1 fs time step. No geometric symmetry was imposed while the cell sizes of L_3, L_1 and L'_1 were fixed to the corresponding cell sizes optimized on the ES at 0 K. (See Table S6)

ES NA transition dynamics simulations at 300 K : The NA transition dynamics among the defect orbitals were simulated based on the time-domain density functional theory

with adiabatic Kohn-Sham (KS) bases.[2] The original diabatic KS orbitals can be expanded by the adiabatic KS orbitals as,

$$\psi_p(\mathbf{r},t) = \sum_{k=1}^{N} c_{pk}(t)|\phi_k(\mathbf{r};\mathbf{R})\rangle, \tag{1}$$

for $p = 1, \cdots, N$. Here, N is the number of electrons to be calculated. The adiabatic KS orbital $\phi_k(\mathbf{r};\mathbf{R})$ corresponding to a defect orbital k depends on time through the time-dependence of $\mathbf{R}(t)$, and can be obtained for atomic positions at each time step along the AIMD trajectories. Substitution of this expanded form into the time-dependent Schrödinger equation leads to the equations of motion for the expansion coefficients in eq.(1),

$$i\hbar\frac{\partial c_{pk}(t)}{\partial t} = \sum_{m=1}^{N} c_{pm}(t)(\epsilon_m\delta_{km} - i\hbar\mathbf{d}_{km}\cdot\dot{\mathbf{R}}). \tag{2}$$

The eigen energies ϵ_m corresponding to fluctuating defect orbital energies can be obtained for instantaneous atomic positions along the AIMD simulations. The electron-phonon coupling to cause the NA transitions among the defect orbitals,

$$\mathbf{d}_{km}\cdot\dot{\mathbf{R}} = \langle\phi_k(\mathbf{r};\mathbf{R})|\nabla_{\mathbf{R}}|\phi_m(\mathbf{r};\mathbf{R})\rangle\cdot\dot{\mathbf{R}} = \langle\phi_k(\mathbf{r};\mathbf{R})|\frac{\partial}{\partial t}|\phi_m(\mathbf{r};\mathbf{R})\rangle, \tag{3}$$

stems from the dependence of the adiabatic KS orbitals on the time-dependent phonon dynamics $\mathbf{R}(t)$. The current electron-phonon coupling depends on orbitals as well as on time fluctuating at ambient temperature. Since the electron-phonon coupling is proportional to the phonon velocity, $\dot{\mathbf{R}}$, the current NA transition dynamics would never happen under the Born-Oppenheimer approximation with stationary atoms.

The current NA transition dynamics is spin-dependent and takes place only among the defect orbitals which have a down-spin electron because the defect orbitals which have an up-spin electron as well as the VB are now fully occupied and quiet. Therefore, by extending the previous NA transition dynamics simulation method, we specifically extracted and calculated

the adiabatic KS orbitals, their eigen energies and the electron-phonon couplings related only to the down-spin defect orbitals. Our NA dynamics simulations were performed by directly solving the equations of motion, eq.(2), with the time-dependent electron-phonon couplings, eq.(3), and the defect orbital energies, ϵ_m, for the ES down-spin defect orbitals 1021-1024 in L_3, L_1 and L'_1. The initial expansion coefficient of the defect orbital 1021 was set as unity while the other expansion coefficients were set as zero. 2700 initial conditions were sampled from the 3 ps AIMD trajectory to get the converged real-time population dynamics shown in Fig.5.

Data Analysis : All the defect orbitals were computed by VASP. The calculated defect orbitals were visualized by XCrySDen2 with the isovalue of 0.025.[10] The time-averaged orbital energies at 300 K were obtained by averaging each orbital energy along the 3 ps microcanonical trajectories obtained by the AIMD simulations at 300 K. Atomic coordinates at each step of the 3 ps AIMD trajectories were obtained by adjusting the xyz-coordinates of the whole structure to the center of mass at each step. Time-averaged atomic coordinates were rendered from averaging out the adjusted xyz-coordinates of corresponding atoms over the 3 ps AIMD trajectories at 300 K. Time-dependent xyz-coordinates of vacancy sites were calculated according to the translational symmetry of the diamond lattice. The lattice points were derived from C atoms far from the NV defects at each step of the 3 ps AIMD trajectories at 300 K.[11] Then, the time-dependent C-V and N-V distances in the NV defects were estimated from the corresponding relative xyz-coordinates between the two vacancies and the eight core atoms of the two defects at each time step. The RSDs and RMSDs were obtained by comparing xyz-coordinates of the eight core atoms in the two NV defects on the GS at 0 K and on the ES at 0 K and 300 K. The atomic coordinates on the ES at 300 K are the time-averaged atomic coordinates as explained above. The RSD and RMSD values were

calculated by setting the corresponding atomic coordinates on the ES at 0 K as a reference.

---

[1] G. Kresse and J. Furthmüller, Phys. Rev. B **54**, 11169 (1996).

[2] R. Ulbricht, S. Dong, I.-Y. Chang, B. M. K. Mariserla, K. M. Dani, K. Hyeon-Deuk, and Z.-H. Loh, Nat. Commun. **7**, 13510 (2016).

[3] D. E. Vanpoucke and K. Haenen, Diam. Relat. Mater. **79**, 60 (2017).

[4] K. Czelej, K. Ćwieka, P. Śpiewak, and K. J. Kurzydłowski, J. Mater. Chem. C **6**, 5261 (2018).

[5] J. Davidsson, V. Ivády, R. Armiento, T. Ohshima, N. T. Son, A. Gali, and I. A. Abrikosov, Appl. Phys. Lett. **114**, 112107 (2019).

[6] G. Thiering and A. Gali, Phys. Rev. B **94**, 125202 (2016).

[7] E. A. Ekimov, P. S. Sherin, V. S. Krivobok, S. G. Lyapin, V. A. Gavva, and M. V. Kondrin, Phys. Rev. B **97**, 045206 (2018).

[8] Y. Ma, M. Rohlfing, and A. Gali, Phys. Rev. B **81**, 041204 (2010).

[9] J. Zhang, C.-Z. Wang, Z. Z. Zhu, and V. V. Dobrovitski, Phys. Rev. B **84**, 035211 (2011).

[10] A. Kokalj, Comp. Mater. Sci. **28**, 155 (2003).

[11] R. Ulbricht, S. Dong, A. Gali, S. Meng, and Z.-H. Loh, Phys. Rev. B **97**, 220302 (2018).